THE HONG KONG
POLYTECHNIC UNIVERSITY
香港理工大學
Pao Yue-kong Library
包玉剛圖書館

Copyright Undertaking

This thesis is protected by copyright, with all rights reserved.

By reading and using the thesis, the reader understands and agrees to the following terms:

1. The reader will abide by the rules and legal ordinances governing copyright regarding the use of the thesis.
2. The reader will use the thesis for the purpose of research or private study only and not for distribution or further reproduction or any other purpose.
3. The reader agrees to indemnify and hold the University harmless from and against any loss, damage, cost, liability or expenses arising from copyright infringement or unauthorized usage.

IMPORTANT

If you have reasons to believe that any materials in this thesis are deemed not suitable to be distributed in this form, or a copyright owner having difficulty with the material being included in our database, please contact lbsys@polyu.edu.hk providing details. The Library will look into your claim and consider taking remedial action upon receipt of the written requests.

Pao Yue-kong Library, The Hong Kong Polytechnic University, Hung Hom, Kowloon, Hong Kong

http://www.lib.polyu.edu.hk

EVALUATION OF THE PULMONARY PERFUSION GENERATED BY DEEP LEARNING-BASED ENHANCED CBCT

WU YUYAO

MPhil

The Hong Kong Polytechnic University

2026

The Hong Kong Polytechnic University

Department of Health Technology and Informatics

Evaluation of the Pulmonary Perfusion Generated by Deep Learning-based Enhanced CBCT

WU Yuyao

A thesis submitted in partial fulfilment of the requirements for the degree of Master of Philosophy

August 2025

CERTIFICATE OF ORIGINALITY

I hereby declare that this thesis is my own work and that, to the best of my knowledge and belief, it reproduces no material previously published or written, nor material that has been accepted for the award of any other degree or diploma, except where due acknowledgement has been made in the text.

_____ (Signed)

WU Yuyao_____(Name of student)

Abstract

Introduction:

With the emerging Cone Beam Computed Tomography (CBCT) enhancement technology, the image quality of CBCT can be improved to a level comparable to Computed Tomography (CT), making it a potential alternative to CT for assessing pulmonary lung function in functional lung avoidance radiotherapy (FLART). However, research on CBCT-based functional image translation is limited, with most studies focusing on translating 4D CBCT to ventilation images. This study aims to evaluate perfusion images generated by enhanced CBCT, quantify their correlation with CT-based perfusion images, and analyze the factors that may affect their clinical application.

Methods:

In this project, thirty lung cancer patients with CBCT-CT pairs and Single-Photon Emission Computed Tomography (SPECT) perfusion images were studied. A previously developed Cycle GAN CBCT enhancement model and a 3D CNN CT-to-perfusion model were utilized to generate perfusion images. Both CBCT images and SPECT perfusion images were registered to the corresponding CT images for further process. Registered CBCT images were input into the Cycle GAN model to produce enhanced CBCT (eCBCT) images. Subsequently, the lung mask generated from CBCT was applied to CBCT, eCBCT, CT, and SPECT images, generating $CBCT_{segCBCT}$, $eCBCT_{segCBCT}$, $CT_{segCBCT}$, and $SPECT_{segCBCT}$. Additionally, the CT lung mask was applied to CT and SPECT images for comparison, resulting in CT_{segCT} and $SPECT_{segCT}$.

Then all 4 sets of CT images ($CBCT_{segCBCT}$, $eCBCT_{segCBCT}$, $CT_{segCBCT}$, CT_{segCT}) were translated into perfusion images using the 3D CNN network. Evaluation metrics, including Spearman's correlation coefficient R and structural similarity index measure (SSIM) for voxel-wise agreement and dice similarity coefficient (DSC) for function-wise agreement, were calculated between the generated perfusion images and their corresponding ground truth SPECT images.

Results:

After enhancement, the SSIM between CBCT and CT has increased from 0.804±0.072 to 0.824±0.068, while the PSNR increased from 24.16±2.82 to 25.04±2.88. Furthermore, the MAE decreased from 47.75±15.95 to 40.13±14.61, showing that the eCBCT has higher voxel-wise agreement with CBCT. For CT-to-perfusion translation, the average Spearman correlation R for $CBCT_{segCBCT}$, $eCBCT_{segCBCT}$, and $CT_{segCBCT}$, and CT_{segCT} were 0.64, 0.68, 0.73, 0.76, and the average SSIM were 0.62, 0.78, 0.76, 0.79, respectively. Function-wise evaluation of generated perfusion images showed a moderate agreement with the ground truth and the 4 sets had similar results, with DSC (High function) around 0.62 and DSC (Low function) around 0.69. In general, the order of performance from best to worse is: CT_{segCT}, $CT_{segCBCT}$, $eCBCT_{segCBCT}$, and $CBCT_{segCBCT}$, as expected.

Conclusion:

In this study, pulmonary perfusion images were generated from CBCT images, demonstrated the potential application of CBCT-based functional images in FLART.

Although reducing noise and artifacts in CBCT images can enhance the accuracy of CT-to-perfusion translation and produce perfusion images with a roughly similar pattern, the incomplete lung regions in CBCT, due to limited fields of view, affect the performance of the CT-based translation model.

Acknowledgement

I want to sincerely thank everyone who supported me throughout my education.

First and foremost, I am deeply grateful to my supervisor, Prof. Cai, for his constant guidance and patient support. I also owe thanks to my classmates and colleagues in Prof. Cai's team. Then, I would like to thank my parents for giving me quiet time and sending me encouraging messages, and your emotional reassurance during exams and deadlines meant more than I can express. Finally, I want to acknowledge the administrative and technical staff at PolyU for their behind-the-scenes work, from troubleshooting software issues to guiding me through submission procedures. Every small act of help added up and kept this project moving forward.

Table of Contents

Chapter 1 Introduction

Research about functional lung avoidance radiotherapy (FLART) was reviewed to provide essential background information in Section 1.1. In section 1.2, research about common imaging modalities for pulmonary perfusion imaging was carefully studied. Section 1.3 reviewed recent research on Cone Beam Computed Tomography (CBCT)-to-CT and CBCT-to-functional images translation to analyze the factors that may affect translation performance.

1.1 Functional Lung Avoidance Radiotherapy

Lung cancer is the most common cause of cancer-related death worldwide (1). One important treatment method for lung cancer is radiotherapy, which uses high-energy radiation beams to kill tumor cells or prevent tumor progression. However, radiation can also damage healthy cells surrounding tumor, leading to serious side effects such as radiation pneumonitis and pulmonary fibrosis (2). To reduce the risk of these radiation-induced lung injuries (RILI), a promising approach is FLART, which integrates functional lung information into the treatment planning process. By minimizing the dose delivered to high-functioning lung regions, FLART has demonstrated the ability to better preserve patients' lung function and reduce the risk of RILI (3).

Several functional imaging techniques can be used in FLART, including single-

photon emission computed tomography (SPECT) (4), positron emission tomography (PET) (5), and hyperpolarized gas magnetic resonance (MR) imaging (6). By integrating these functional imaging modalities, FLART can assess the functional status of the lungs in the presence of the tumor. By identifying regions of viable lung function, clinicians can strategically increase the radiation dose to poorly ventilated and perfused regions while reducing the dose to highly functional areas. This approach helps decrease the incidence of radiation pneumonitis and pulmonary fibrosis, thereby preserving the patient's lung function and minimizing dyspnea and quality of life deterioration after treatment (4,7,8). Additionally, by sparing high-functioning lung regions, a higher dose can be delivered to the tumor area, which enhances the effectiveness of cancer cell eradication and improves the patient's survival rate.

Ventilation and perfusion imaging can be utilized in FLART to assess the functional status of the lung regions by reflecting the gas exchange and blood supply, respectively. The ventilation/perfusion (V/Q) ratio represents the effectiveness and adequacy of the ventilation-perfusion coupling (9). However, a V/Q mismatch can occur during the radiotherapy treatment process. For instance, airway obstruction due to tumor progression or atelectasis resulting from respiratory infection caused by pulmonary comorbidities can lead to a decrease in effective ventilation. And the decrease in perfusion may result from bleeding in pulmonary capillaries or pulmonary embolism (10). Because vascular endothelial cells are one of the most

radiation-sensitive cells in the lungs (11), perfusion is considered to be a more sensitive indicator in radiotherapy treatment for accessing lung function and the risk of RILI.

Currently, most FLART clinical trial protocols only scan functional images once for treatment planning (12). However, lung function can change throughout the treatment process due to disease progression and the delivered radiation dose, which can alter lung ventilation or perfusion. This single-scan approach overlooks the impact of lung function changes between different treatment fractions, potentially affecting the overall treatment outcome. Meng et al. analyzed SPECT ventilation and perfusion images of 15 Non-small cell lung cancer (NSCLC) patients during radiotherapy and observed significant improvements in local ventilation and perfusion function (13). Additionally, research using ventilation images generated by 4D-CT reported that 3 out of 6 patients showed improved ventilation after receiving a dose, while the others either experienced a decrease or no change (14). This patient-specific pattern was also noted in another study involving nine lung cancer patients (15). Similarly, Kipritidis et al. examined lung function changes in 19 patients with locally advanced non-small cell lung cancer during 4-6 weeks of radiotherapy using ventilation images generated from 4D-CBCT (16). The research found that all patients experienced both positive and negative changes with varying patterns, and at least one subsequent change in median ipsilateral ventilation was ≥10%. Changes in lung function during treatment can generally be categorized into

decreases due to regional radiation-induced lung injury and increases resulting from the restoration of airway patency and blood circulation following radiation-induced tumor shrinkage (17,18). To effectively manage these changes and optimize the performance of FLART, it is advantageous to implement adaptive strategies that allow treatment plans to be updated based on lung function changes between fractions. Yamamoto et al. demonstrated the benefits of plan adaptation, showing that by modifying the subsequent doses in the plan at 20 Gy and 34 Gy, the functionally weighted mean lung dose (fMLD) was decreased by 6.1% to 14.3%, respectively, compared to the plans without adaptation (19). This adaptive approach enables patients to receive more precise and personalized radiotherapy treatment.

1.2 Perfusion Imaging Modalities

Perfusion imaging can be directly obtained through SPECT, PET, and MR. Among these, technetium-99m labeled macroaggregated albumin (MAA) SPECT perfusion is the most thoroughly studied method for collecting the functional data essential for function-guided lung avoidance treatment planning (12). While SPECT is valuable, it does come with certain drawbacks, including patient exposure to ionizing radiation and lower spatial and temporal resolution compared to CT, MR, or PET (20). Additionally, challenges such as errors in attenuation and scatter correction (21), as well as difficulties in aligning functional data with CT images (22) and maintaining consistent patient positioning and breathing patterns, can arise.

In contrast, PET perfusion imaging using gallium-68 MAA offers a fully quantitative approach with the added benefit of respiratory correlation analysis (5). However, the significant cost associated with PET imaging limits its widespread adoption in clinical practice.

Hyperpolarized gas MR imaging emerges as a promising, radiation-free alternative to traditional nuclear medicine imaging, offering a more detailed analysis of lung function. Research has analyzed the performance of FLART based on hyperpolarized gas MR and showed satisfactory results (4,6,23). Despite its potential, several obstacles impede its clinical use in radiotherapy, including the availability and cost of gases, the specialized expertise and equipment required, and the need for precise image co-registration with planning CT. Furthermore, innovative MR lung imaging techniques are being developed to eliminate the need for pre-polarized gases (24). New instruments for multi-core single-shot breath-hold imaging are enhancing the co-registration of gas MR with CT images (25,26).

Additionally, deriving functional lung imaging from CT has also attracted widespread interest due to its availability. CT is a fundamental tool in radiation therapy treatment planning due to its precise geometric accuracy and its ability to provide electron density information essential for dose calculations. Its widespread availability makes CT-derived functional images more accessible compared to those from SPECT, PET, or MR. Furthermore, since CT scanning is the predominant imaging modality for treatment planning, CT-based functional imaging eliminates

the need for additional scanning in FLART. Historically, plain film X-ray has been used in clinical settings to assess lung blood flow by examining variations in the size of the pulmonary vasculature and the differing levels of transparency in various lung regions. For multidetector computed tomography (MDCT), lung perfusion is still estimated by evaluating local variations in lung density, specifically through attenuation values measured in Hounsfield units (HU) (27).

Various CT-based image processing techniques have been explored to provide functional data for treatment planning. Current research on the application of CT in FLART mainly focused on generating ventilation images from 4D-CT by assessing the volume changes of the lung between the inhale and exhale phases. Techniques such as breath-hold imaging or 4D-CT, often combined with deformable image registration, are used to generate ventilation maps based on Jacobi or Hounsfield units (28–31). However, implementing 4D-CT requires substantial investment in respiratory equipment and expertise, and it exposes the entire lung to higher radiation doses than standard 3D planning CT. Recently, deep learning-based algorithms for CT-to-ventilation translation were also developed and demonstrated comparable performance with the traditional DIR-based methods (32,33). Despite the advantages, these methods do not consistently provide robust voxel-level functional information, and different image registration algorithms can significantly impact the generated ventilation values (34). As for the CT-perfusion translation, Castillo et al. formulated the explicit voxel-wise relationship between HU and

perfusion parameters in non-contrast 4D-CT using their DIR-Jac algorithm incorporated with respiration-induced blood-mass volume changes (35). Ren et al. developed the first 3DCT-to-perfusion deep learning translation model and a transfer learning framework for this model to generate perfusion images for lung cancer patients, proving the feasibility of utilizing CT-based perfusion in FLART (36,37). Compared with CT-to-ventilation translation, further research is needed for CT-to-perfusion translation.

1.3 CBCT

Cone-beam CT is a commonly used image guidance tool in clinical practice because of its high spatial resolution in the axial plane and low radiation dose. It is an on-board imaging technique and has a fast-imaging speed (38). In clinic, a routine CBCT is performed before each radiotherapy treatment fraction to verify the patient's position, ensuring the accuracy of treatment. In addition, the purchase and maintenance costs of CBCT equipment are relatively low, and it is easy to operate, making it suitable for widespread use in clinical settings. However, compared with spiral CT, CBCT has lower soft tissue contrast resolution, which may affect the identification and evaluation of certain lesions. CBCT images are also more susceptible to factors such as metal implants, motion, and scattering, which can produce artifacts and affect image quality (39).

To enhance the image quality of CBCT slices, traditional methods for minimizing

scattered photons often rely on anti-scatter grid hardware and scatter deconvolution estimation (40). Although these techniques can reduce artifacts to some extent, they are typically computationally intensive and provide only moderate improvements. To address these limitations, innovative iterative projection reconstruction methods have been developed, significantly enhancing CBCT image quality. However, it is important to note that while these methods are highly effective, they may occasionally compromise the clarity of anatomical details and generally require access to the original projection data.

Recently, advancements in artificial intelligence (AI) modeling have successfully elevated the quality and accuracy of CBCT images to a level comparable to CT image (41). This improvement indicates the possibility of utilizing algorithms similar to those employed in CT-to-functional image translation to generate CBCT-based functional images. Since CT images are routinely acquired in radiotherapy for treatment planning, it is straightforward to collect CT-CBCT image pairs for deep learning model training. Common deep learning architectures include U-Net, generative adversarial network (GAN), and Cycle GAN. U-Net offers the simplest implementation and the fastest training speed. U-Net based models typically utilize a pixel-wise loss function to minimize the differences between CBCT and paired CT images. Therefore, accurate registration between CBCT and CT images is necessary to achieve satisfactory performance. Compared to U-Net, GAN can provide improved model tunability and image realism due to its competitive

generator-discriminator setting. And Cycle GAN, which consists of two GANs, incorporate a cycle-consistency loss to preserve the anatomical information in the original CBCT images and have become the most popular architecture in recent years (41). Research reported satisfactory CBCT enhancement using Cycle GAN models at different anatomical sites. This research paved the foundation of potential CBCT-to-functional image translation. By applying similar approaches in CT-to-functional image translation to the enhanced CBCT images, pulmonary functional images can be derived from routine CBCT and employed in FLART.

CBCT-based functional images enable the inter-fractional and intra-fractional lung function assessment in FLART. Plan adaptation can be made based on the lung function changes in routine CBCT-derived ventilation or perfusion images. Research reported that improving 4D-CBCT image quality by applying projection correction and reconstruction algorithms can subsequently improve the ventilation image quality derived from CBCT (42). Woodruff et al. showed reasonable to good voxel-level agreement between DIR based ventilation images derived from 4D-CBCT and those derived from 4DCT (15). Deep learning based 4D-CBCT-to-ventilation model was also developed and showed an improved performance compared to DIR-based methods (43). However, research on CBCT-based functional images remains limited and has primarily focused on translating 4D CBCT data into ventilation images. The reliance on 4D CBCT also reduces the accessibility of this technique in FLART. On the other hand, there is only one

research reported the feasibility of 3D CBCT-to-perfusion translation using cascaded deep learning framework (44). Further research is required to comprehensively evaluate the factors that influence the performance of CBCT-to-perfusion translation.

1.4 Significance of this study

The studies discussed above demonstrate that a functional lung avoidance strategy can significantly improve treatment outcomes for lung cancer patients undergoing radiotherapy. By limiting the dose delivered to high-function lung regions, the risk of radiation-induced lung injury, including radiation pneumonitis and pulmonary fibrosis, can be reduced, thereby enhancing patients' quality of life. Common functional imaging techniques such as SPECT, PET, and MRI require specialized equipment and impose additional financial burdens on patients, limiting their accessibility. As an alternative, CT-based functional image acquisition has gained popularity due to its routine inclusion in standard care for patients during radiotherapy planning. Research indicates that both DIR-based and deep learning-based CT-to-functional image translation models perform satisfactorily, suggesting that CT can be a suitable candidate for functional imaging in FLART. However, the current single-scan FLART protocol does not account for changes in lung function between fractions, which may impact treatment outcomes. Considering this, CBCT has the potential to monitor lung function changes during radiotherapy and trigger plan adaptations in FLART. By applying algorithms similar to CT-to-

functional image translation to routine CBCT, inter-fraction and intra-fraction functional information can be obtained without additional imaging procedures. While the reproducibility of ventilation images between CBCT and CT has been verified, there is still a lack of research on the differences between perfusion images generated by CBCT and CT. Therefore, in this study, the differences between CBCT-based and CT-based pulmonary perfusion images were quantified and analyzed to provide insight into possible applications of CBCT-based perfusion in FLART.

1.5 Objectives of this study

This project aims to evaluate pulmonary perfusion images translated from deep learning-enhanced CBCT. The differences between CBCT-generated and CT-generated perfusion images will be analyzed both qualitatively and quantitatively.

1.6 Organization of this dissertation

In this dissertation, Chapter 1 provides a comprehensive literature review of related studies on FLART and functional imaging and states the objectives of this study. Chapter 2 explains the data processing pipeline in this study. Chapter 3 demonstrates and analyzes the results. Chapter 4 concludes the whole dissertation.

Chapter 2 Methodology

2.1 Data Preprocessing

A total of 30 lung cancer patients (27 male, 3 female) from Henan Tumor Hospital were studied, 28 of whom were older than 53 years old. Each patient has a planning CT, a series of fractional CBCTs, and a SPECT scanned within 7 days of the planning CT scanned. The CBCT before the first fraction was used for the following perfusion image generation.

The planning CTs were acquired on a Brilliance Big Bore scanner (Philips Medical Systems) while CBCT images were acquired on a VitalBeam LINAC (Varian Medical Systems). Each CT image was reconstructed into 512×512 slices with 1.172×1.172 mm^2 in-plane pixel spacing and 3 mm slice spacing, and each CBCT image was reconstructed into a 512×512 slices with 0.511×0.511 mm^2 in-plane pixel spacing and 1.99 mm slice spacing. The SPECT perfusion images were acquired on a Discovery NM/CT 670 CZT scanner, and each SPECT image was reconstructed into a 128 × 128 × 128 matrix with a voxel size of 4.42 × 4.42 × 4.42 mm^3.

Figure 1 shows the flowchart of image processing pipeline in this project. First, all data was resampled to 1×1×1 mm^3 voxel size for further processing. Then both the CBCT and SPECT images were registered to the corresponding CT images using a B-spline transformation algorithm implemented in the Elastix module (45,46) in 3D Slicer software (47). Lung segmentation was performed using the open-source U-

Net model (48). And the tumor regions were masked out using the planning target volume (PTV) contours derived from the corresponding planning CT. The lung masks generated from CBCT images were applied to CBCT, CT, and perfusion images for major evaluation. The results were denoted by $CBCT_{segCBCT}$, $CT_{segCBCT}$, and $SPECT_{segCBCT}$. Additionally, because most of the CBCT images don't include the whole lung region, lung masks generated from CT images were also applied to CT and perfusion images to evaluate the impact of lung region integrity in CT-to-perfusion translation. The results were denoted by CT_{segCT}, and $SPECT_{segCT}$.

For CBCT enhancement, $CBCT_{segCBCT}$ was input into the Cycle GAN CBCT enhancement model, generating $eCBCT_{segCBCT}$. $CT_{segCBCT}$ was used as the ground truth of CBCT enhancement. For CT-to-perfusion translation, $CBCT_{segCBCT}$, $eCBCT_{segCBCT}$, $CT_{segCBCT}$, and CT_{segCT} were resampled to 128 × 64 × 64 matrices then input into the 3D CNN model. The output perfusion images were denoted by $PI\_CBCT_{segCBCT}$, $PI\_eCBCT_{segCBCT}$, $PI\_CT_{segCBCT}$, and PI_CT_{segCT}, as illustrated in Figure 1.

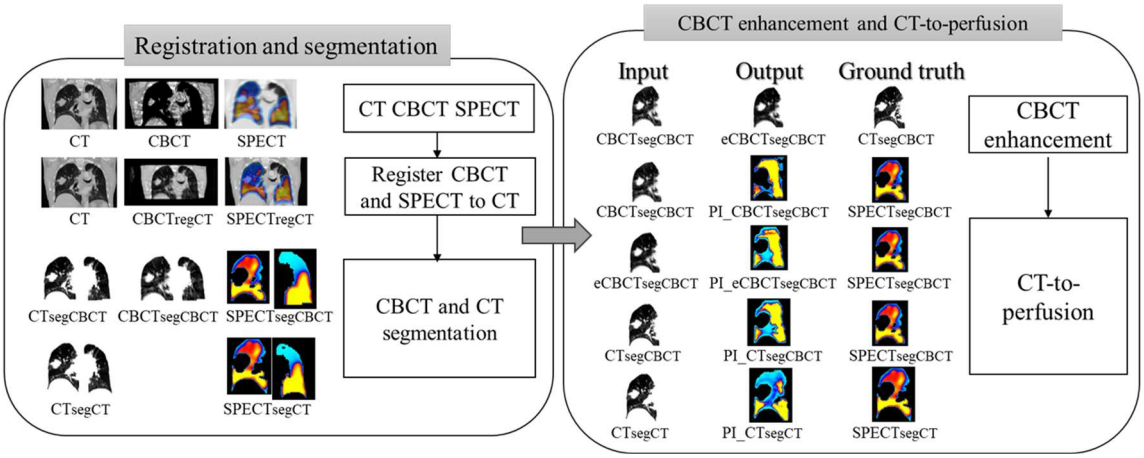

Figure 1. Flowchart of the image processing pipeline

2.2 CBCT Enhancement

A previously developed 2D Cycle GAN model was used to reduce the artifacts in CBCT images and enhance the image quality of CBCT to CT level (44). The model was trained on 106 CBCT-CT pairs for lung cancer patients from Queen Mary Hospital in Hong Kong. Commonly used adversarial loss, cycle consistency loss and identity loss were employed in this model for stable optimization, additionally with a synthetic loss for training acceleration considering the limited training dataset size (49–52). This model achieved a MAE of 47.06±11.31HU and a PSNR of 24.08±1.76 on the testing dataset. CBCT images were inputted into this model to generate the enhanced CBCT images denoted by eCBCT.

2.3 CT-to-Perfusion Translation

The CT-to-Perfusion translation was performed using the 3D CNN model developed by Ren et al. (36). This model was first trained on a dataset of 73 patients with suspected lung diseases from Queen Mary Hospital and then a transfer learning framework was performed to adapt the model to the lung cancer patients specifically. The transfer learning framework utilized a dataset of 33 lung cancer patients and 137 non-cancer patients from Hong Kong Queen Mary Hospital (14 lung cancer cases and 137 non-cancer cases) and Henan Cancer Hospital (19 lung cancer cases). The model used an attention residual neural network (ARNN) to extract texture features and reconstruct perfusion images. A binary cross-entropy loss was used to

improve the model sensitivity to small lung regions with low function. This model demonstrated well agreement between the SPECT and generated perfusion, with a high voxel value correlation (Spearman's correlation coefficient R = 0.8142 ± 0.0669) and high function-wise correlation (Dice Similarity Coefficient DSC = 0.8112 ± 0.0484 for high-function lung regions and 0.8137 ± 0.0414 for low-function lung regions).

2.4 Evaluation

To evaluate the performance of CBCT enhancement, voxel-to-voxel comparisons on CBCT/CT pairs and eCBCT/CT pairs were conducted separately. MAE was calculated using Eq. (1) to assess absolute voxel-wise differences. Peak signal-to-noise ratio (PSNR) was computed by Eq. (2) to evaluate the degree of noise reduction in the eCBCT image. Structural similarity index (SSIM) was calculated by Eq. (3) to quantify image quality perception and pattern matching based on the human visual system: luminance $L(X,Y)$, contrast $C(X,Y)$, and structure $S(X,Y)$.

$$MAE(X,Y) = \frac{1}{n}\sum_{i,j,k}\left|X_{i,j,k} - Y_{i,j,k}\right| \quad (1)$$

$$PSNR(X,Y) = 20\log_{10}\left(\frac{MAX}{MSE}\right) \quad (2)$$

$$SSIM(X,Y) = L(X,Y) \times C(X,Y) \times S(X,Y) = \frac{(2\mu_X\mu_Y + c_1)}{(\mu_X^2 + \mu_Y^2 + c_1)} \times \frac{(2\sigma_X\sigma_Y + c_2)}{(\sigma_X^2 + \sigma_X^2 + c_2)} \times \frac{(2\sigma_{XY} + c_2)}{(2\sigma_X\sigma_Y + c_2)} \quad (3)$$

where $X_{i,j,k}$, $Y_{i,j,k}$ represent the pixel values of images X and Y at coordinates

(i, j, k). n refers to the total voxel number of the image. μ_X, σ_X denote the mean and standard deviation of image X. σ_{XY} is the covariance of image X and Y. c_1, c_2 are two regularization constants. MAX refers to the maximum intensity difference between compared images.

Evaluation of CT-to-perfusion translation was conducted using evaluation metrics including Spearman's correlation *R*, SSIM and DSC. The evaluation was calculated separately on PI_CBCT$_{segCBCT}$/SPECT$_{segCBCT}$, PI_eCBCT$_{segCBCT}$/SPECT$_{segCBCT}$, PI_CT$_{segCBCT}$/SPECT$_{segCBCT}$, and PI_CT$_{segCT}$/SPECT$_{segCT}$ pairs to assess the differences between CBCT-to-perfusion translation and CT-to-perfusion translation. To compare the output performance between different patients, each SPECT perfusion was normalized to its 75th percentile value, which can be considered as the perfusion value of normal function lung (53).

Spearman's correlation R was used to assess the intensity correlation and is calculated by

$$R(X,Y) = \frac{\sum_{i,j,k}\left[\left(X_{i,j,k} - \mu_X\right)\left(Y_{i,j,k} - \mu_Y\right)\right]}{\sqrt{\sum_{i,j,k}\left(X_{i,j,k} - \mu_X\right)^2}\sqrt{\sum_{i,j,k}\left(Y_{i,j,k} - \mu_Y\right)^2}} \quad (4)$$

DSC was computed to evaluate the similarity of functional subgroups (low or high) classification between SPECT images and generated perfusion images. Although the selection of threshold dividing high and low function lung regions is

challenging, this study classified lung region with perfusion intensity above 0.66 as high functional portions, according to previous research (29,36). And DSC is calculated by

$$DSC_i = \frac{2 * |X_i \cap Y_i|}{|X_i| + |Y_i|} \quad (5)$$

where i denotes the functional subgroups (low or high). $|X_i|$, $|Y_i|$ are the functional sub-volumes in images X and Y respectively, while $|X_i \cap Y_i|$ is the mutual sub-volume classified in both images.

To assess the impact of tumor volume on the model's performance, correlation analyses were conducted between the PTVs and two evaluation metrics (correlation R and SSIM). The evaluation metrics calculated between PI_CT_{segCT}/$SPECT_{segCT}$ was used to exclude the impact of truncated lung region in CBCT lung masks. The PTVs was employed as a surrogate for tumor volume, consistent with its use in the pre-processing pipeline where the PTV contour was applied to mask out and exclude the primary tumor region from the CBCT images. For each ipsilateral lung, two distinct volumetric measures were derived: 1) the absolute PTV volume within the lung region (cm^3), and 2) the relative intra-lung PTV volume proportion (%), defined as the intra-lung PTV volume divided by the corresponding lung volume. The relationships between each of these two volumetric measures and the corresponding performance metrics (correlation R and SSIM) were evaluated using linear regression. The strength and statistical significance of the associations were quantified by the Pearson correlation

coefficient (r) and its associated p-value, respectively.

Chapter 3 Results

3.1 CBCT Enhancement

Compared with CBCT, the SSIM between eCBCT and CT has increased from 0.804±0.072 to 0.824±0.068, while the PSNR increased from 24.16±2.82 to 25.04±2.88. Furthermore, the MAE decreased from 47.75±15.95 to 40.13±14.61 after enhancement, showing that the eCBCT has higher voxel-wise agreement with CBCT. Figure 2 and Figure 3 illustrate an example of enhanced CBCT with all metrics close to the average values ($SSIM_{CBCT}$=0.809, $SSIM_{eCBCT}$=0.841, $PSNR_{CBCT}$=22.33, $PSNR_{eCBCT}$=23.95, MAE_{CBCT}=47.46, MAE_{eCBCT}=37.86).

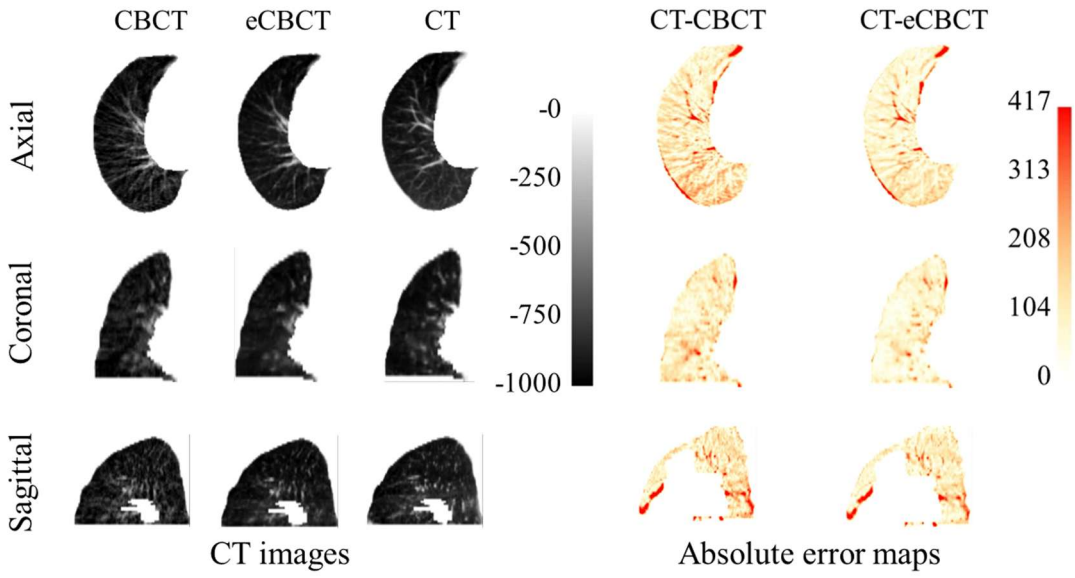

Figure 2. Illustration of the enhanced image quality of eCBCT compared to CT and CBCT with multi-planar views, and the absolute error maps CT-CBCT and CT-eCBCT.

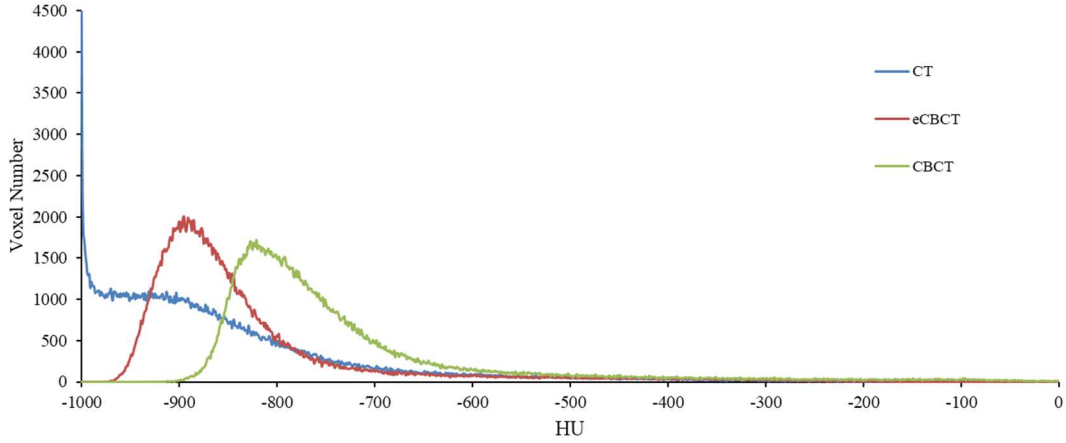

Figure 3. Histogram of the corresponding CT, eCBCT, and CBCT.

Satisfactory reduction of noise and artifacts can be observed in eCBCT, and the absolute errors between eCBCT and CT are reduced compared to errors between CBCT and CT, according to the error maps. However, the reduction of absolute error is slight. One possible reason is that the image quality of the original CBCT image was relatively high so further improvement may be difficult. Moreover, as shown in Figure 2, while the noises were reduced in eCBCT, some anatomical structures in small regions and subtle details were also eliminated, causing a loss of the unique advantages of CBCT and affecting the performance of following image translation. On the other hand, the histogram shows that for HU range in [-800, -500], the histogram of the generated eCBCT is almost the same as the CT image, proving the model's performance. The decrease in voxel number in this range may be caused by the reduction of streaking artifacts. And the peak of CBCT histogram

was shifted from -800 HU to -900 HU after enhancement, improving the HU distribution agreement with CT image.

Overall, the model successfully enhanced the CBCT image to CT level, reducing noises and artifacts. However, the CBCT image quality enhancement extent in this dataset was not as good as that in the model's training dataset (average MAE from 68.99 to 47.06, and average SSIM from 0.84 to 0.89), which indicates potential overfitting of the enhancement model due to the small training dataset. Furthermore, the CBCT enhancement model utilized in this study was pre-trained on data from an external institution (Queen Mary Hospital) with potentially different imaging parameters, which is a limitation. However, as our native CBCT quality was high and the enhancement yielded only marginal gains, its impact was minimal. Crucially, our study focused on relative differences in perfusion, where any systematic bias would be consistent. Thus, we conclude this limitation does not alter our core findings, though future validation with larger datasets is warranted.

3.2 CT-to-Perfusion Translation

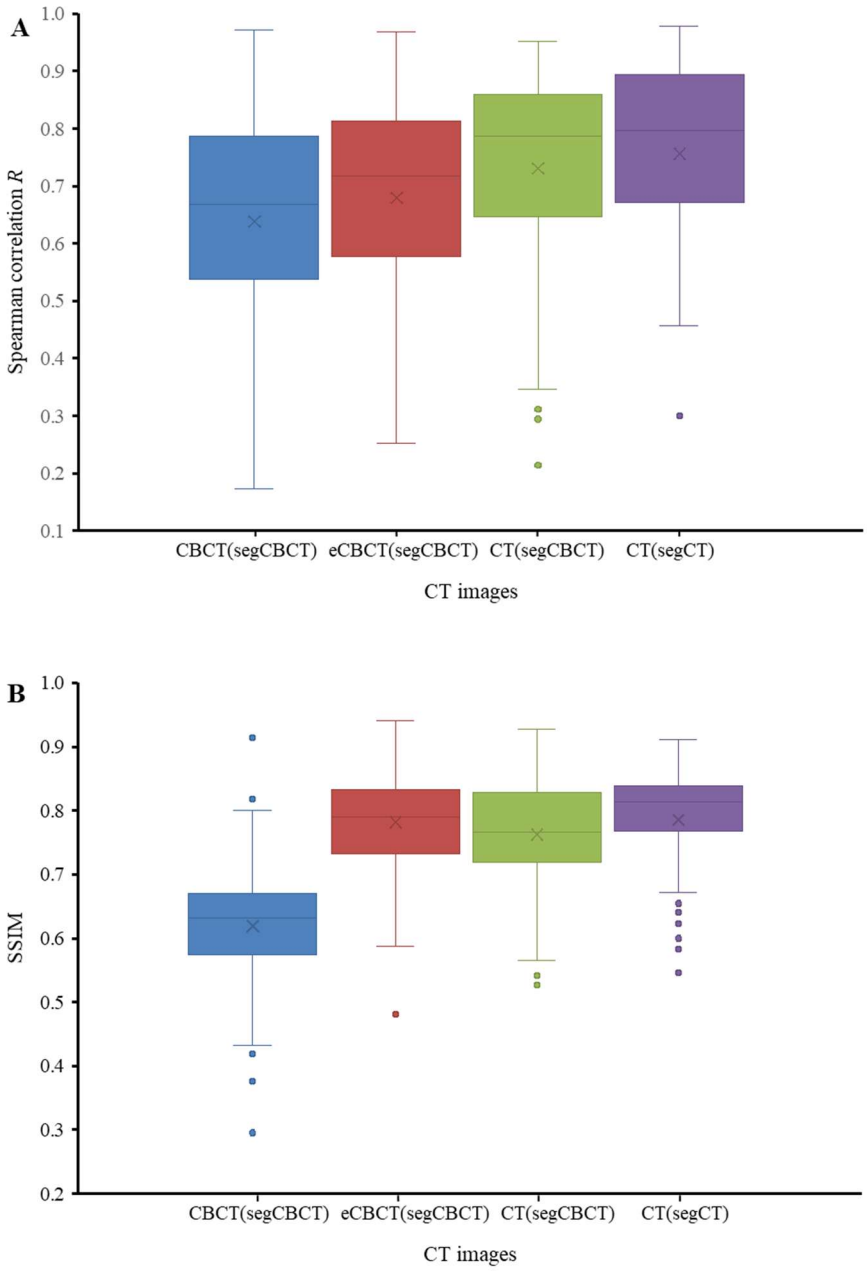

Figure 4. Spearman correlation *R* (A) and SSIM (B) of the generated perfusion images. The lung mask generated from CBCT was applied to $CBCT_{segCBCT}$, $eCBCT_{segCBCT}$, and $CT_{segCBCT}$, and the metrics were calculated with ground truth $SPECT_{segCBCT}$. The lung mask generated from CT was applied to CT_{segCT}, with ground truth $SPECT_{segCT}$.

Figure 4 shows the voxel-wise agreement with corresponding ground truth for the four sets of generated perfusion images. The Spearman correlation R for $CBCT_{segCBCT}$, $eCBCT_{segCBCT}$, $CT_{segCBCT}$, and CT_{segCT} was 0.64±0.20, 0.68±0.11, 0.73±0.19, 0.76±0.17, and the SSIM is 0.62±0.10, 0.78±0.08, 0.76±0.09, 0.79±0.09, respectively.

In general, the perfusion images generated from CBCT images had the lowest voxel-wise correlation with the ground truth, as expected. And the perfusion images generated from CT images with CT lung masks, which include the whole lung region, had the highest correlation. A potential reason is that the CNN model was trained on CT and learned global lung features. Therefore, the incomplete lung region in CBCT image may reduce the model's performance. In addition to the impact of mask choice, the primary findings are derived from a mask-matched comparison. As for the $eCBCT_{segCBCT}$ and $CT_{segCBCT}$, the $CT_{segCBCT}$ had a higher correlation R while the SSIM were almost the same, demonstrating the feasibility of generating reliable pulmonary perfusion images using CBCT images. Similar SSIM indicates that enhanced CBCT images are capable to generate perfusion images with similar levels of perceptual structure with CT images. And the lower correlation R may be due to the different HU distribution of eCBCT and CT, leading to incorrect perfusion values.

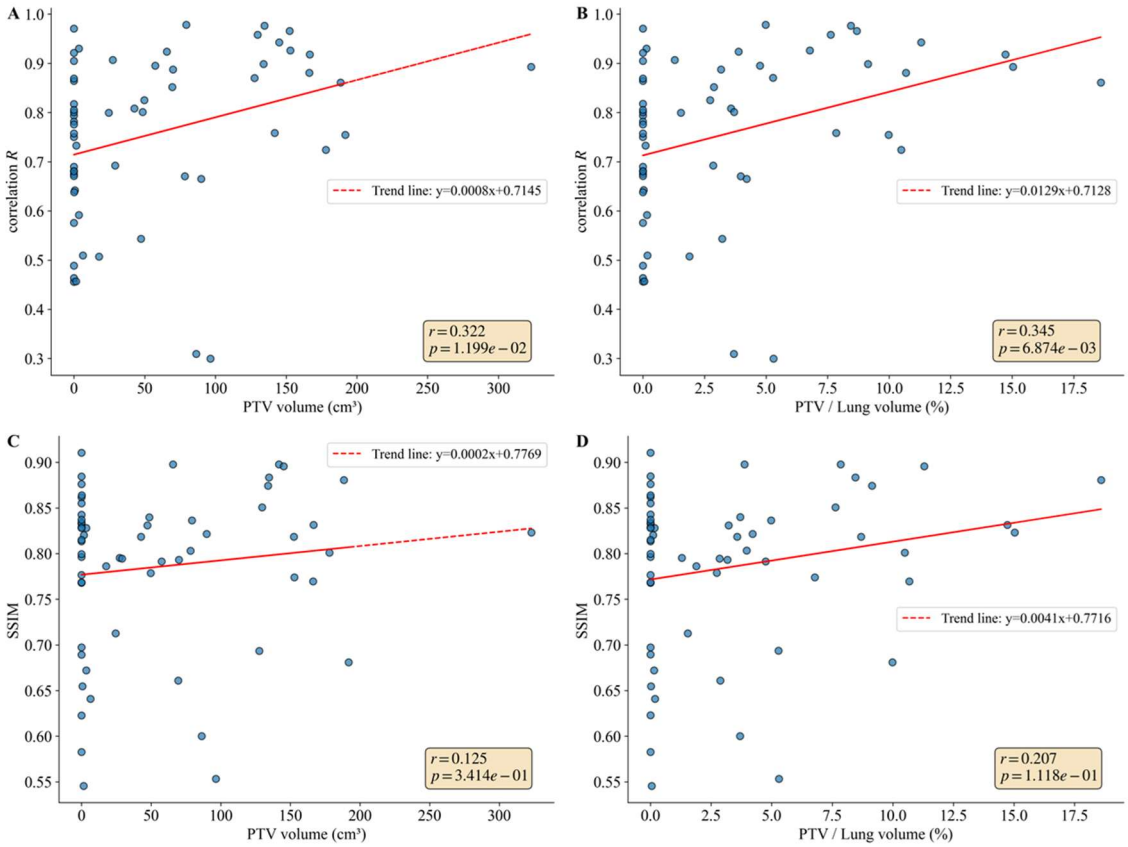

Figure 5. The correlations of model performance and PTV volume. The correlation *R* and SSIM were computed between PI_CT_{segCT} and $SPECT_{segCT}$. Their associations are plotted against (A) the PTV volume within the unilateral lung, and (B) the PTV volume percentage in the unilateral lung. (C) and (D) show the corresponding relationships for the SSIM metric.

Figure 5 presents the relationship between tumor volume, quantified as both the absolute PTV volume within the unilateral lung and its relative volume percentage, and the model's evaluation metrics. The coefficient *R* and the SSIM were computed between PI_CT_{segCT} and $SPECT_{segCT}$, which was segmented using CT lung masks. This design ensures that the model's performance assessment is not confounded by the limited FOV of the CBCT scans, thereby isolating its capability in processing regions with varying tumor burdens.

A weak-to-moderate positive correlation was identified between the global intensity agreement (correlation *R*) and both the PTV volume ($r = 0.322$, $p = 0.012$) and the PTV volume percentage ($r = 0.345$, $p = 0.007$). In contrast, no statistically significant correlation was found between the structural fidelity metric (SSIM) and either volumetric measure (absolute volume: $r = 0.125$, $p = 0.341$; relative proportion: $r = 0.207$, $p = 0.112$). Furthermore, the dataset included 22 cases where the PTV volume was zero, representing the contralateral lung of patients whose tumors are located only in one lung. Notably, within this subset of tumor-free lungs, the model's performance exhibited considerable variance (correlation *R* range: ~0.30 - 0.98; SSIM range: ~0.55 - 0.91). Some of the best and worst-performing cases, for both metrics, were found among these PTV-zero datapoints.

This pattern suggests two primary inferences. First, the significant correlation of PTV volume with correlation *R*, but not with SSIM, implies that tumor burden systematically influences the global intensity scaling of the predicted perfusion map, possibly by altering hemodynamic baselines that the model learns. However, it does not degrade the model's core ability to reconstruct accurate local anatomical texture and structure, which remains robust. Second, the high variance in performance within tumor-free lungs indicates that factors other than tumor presence are major drivers of model accuracy. Key confounding factors may include registration accuracy and patient-specific physiological variations that are not accounted for by the PTV volume. Consequently, while PTV volume explains a small portion of the

variance in global intensity prediction, the model's performance is predominantly governed by these more pervasive technical and biological variables

.

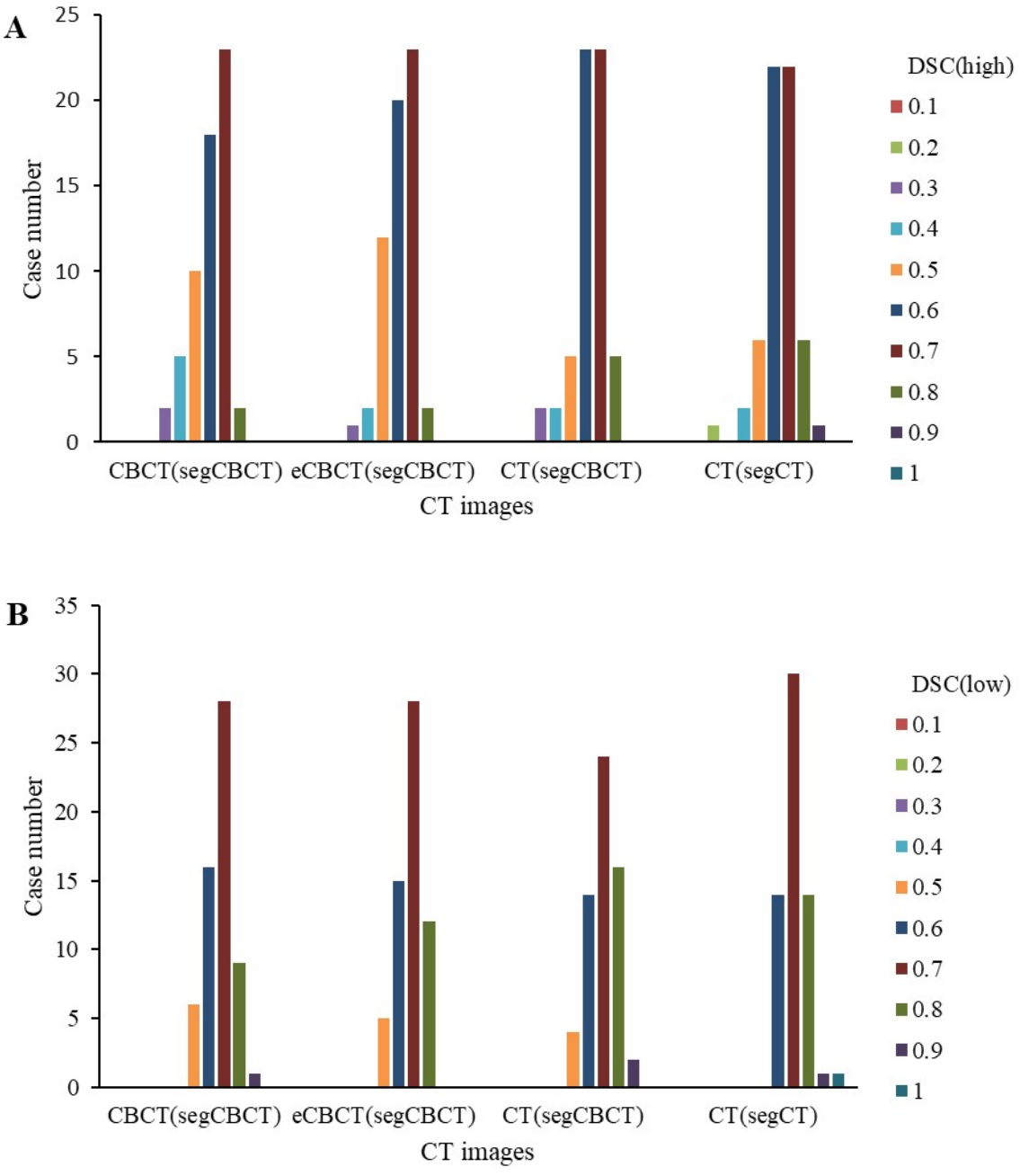

Figure 6. DSC of the generated perfusion images (A: DSC high, B: DSC low). The lung mask

generated from CBCT was applied to $CBCT_{segCBCT}$, $eCBCT_{segCBCT}$, and $CT_{segCBCT}$, and the DSC were calculated with ground truth $SPECT_{segCBCT}$. The lung mask generated from CT was applied to CT_{segCT}, with ground truth $SPECT_{segCT}$.

Figure 6 shows the function-wise correlation of the generated perfusion images. The DSC for high function lung for is $CBCT_{segCBCT}$, $eCBCT_{segCBCT}$, and $CT_{segCBCT}$, and CT_{segCT} was 0.60±0.11, 0.62±0.09, 0.63±0.10, 0.64±0.11, and for low function lung is 0.67±0.09, 0.68±0.08, 0.71±0.09, 0.70±0.08, respectively. Among the 60 cases from 30 patients (left and right lung), 90% of cases achieved DSC higher than 0.6 and 60% achieved 0.7 for low function lung region. For high function region, only 70% achieved 0.6 and 40% achieved 0.7. The generated perfusion images demonstrated a moderate level of function-wise agreement with the ground truth and showed higher agreement in low function lung region. The trend of DSC is consistent with the results of correlation R and SSIM: CT_{segCT}-based perfusion images performed best, followed by $CT_{segCBCT}$ and $eCBCT_{segCBCT}$, and $CBCT_{segCBCT}$ had poor performance. However, the function-wise correlation was lower than that in the published article (~0.8), especially for the CT_{segCT}-based perfusion images, which were supposed to demonstrate similar performance. A potential reason is different data preprocessing methods. Instead of masking out tumors and vessels by limiting the HU value to the range of [-1000, -300] (37), in this study the tumors were removed by using the PTVs contours. Considering the margins in PTVs, more regions may be masked out in this study, affecting the model performance.

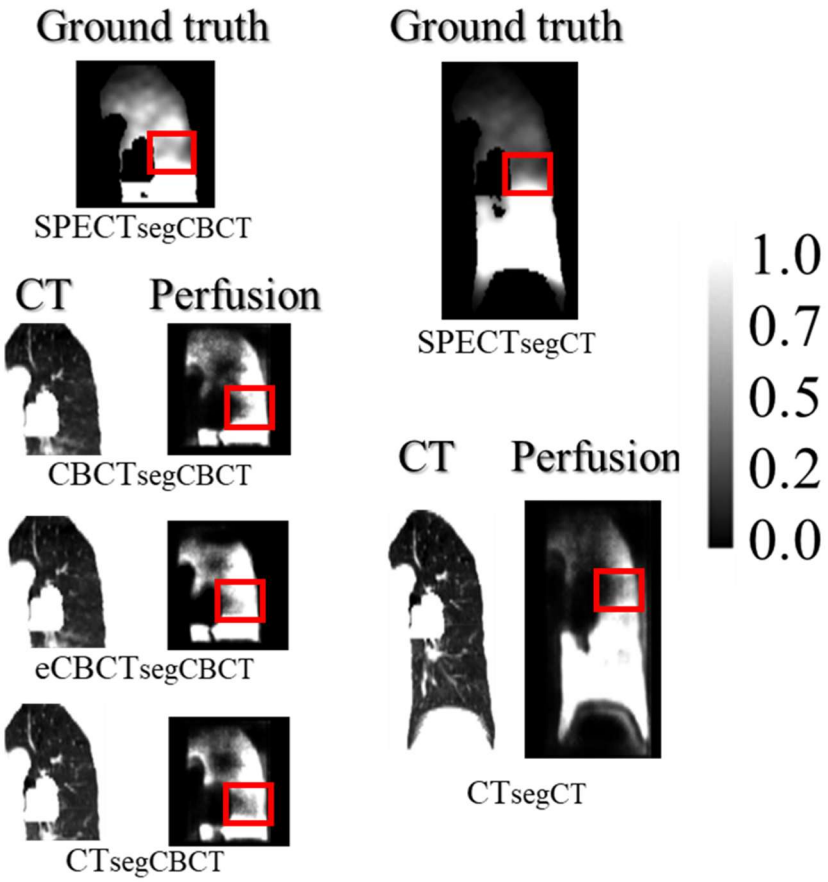

Figure 7. An example of the generated perfusion images and their corresponding CT images and ground truth. The evaluation metrics for this case are listed below.

Table 1. The evaluation metrics for a selected case

	$CBCT_{segCBCT}$	$eCBCT_{segCBCT}$	$CT_{segCBCT}$	CT_{segCT}
R	0.66	0.68	0.69	0.83
SSIM	0.64	0.70	0.70	0.77
DSC(Low)	0.77	0.79	0.80	0.90
DSC(High)	0.63	0.69	0.69	0.83

Figure 7 illustrates an example of generated perfusion images, with the corresponding quantitative metrics provided in Table 1. Overall, PI_CT_{segCT} demonstrates the highest similarity with its corresponding perfusion $SPECT_{segCT}$, while $PI\_CBCT_{segCBCT}$ has the lowest similarity with $SPECT_{segCBCT}$. As indicated by the red square, there is a small low lung function region in the registered SPECT image. PI_CT_{segCT} shows a similar pattern with a higher function region above the red square, while the high function lung region is expanded in the perfusion images generated by CBCT-masked images. On the other hand, in the upper lobe of the lung, a local minimum function region was generated in the CBCT-masked images, which may be due to the smaller field of view of CBCT. Unlike planning CT, which captures the entire lung volume, CBCT's limited FOV can lead to the truncation of peripheral lung anatomy. This truncation causes two key issues: the artificial reduction in image intensity at the FOV boundary and the actual exclusion of lung tissue from the scan. Consequently, the image translation model interprets these truncated areas as having little to no functional signal. Comparing $PI\_CBCT_{segCBCT}$ and $PI\_eCBCT_{segCBCT}$, the major difference is the left boundary in the upper lobe, in which $PI\_eCBCT_{segCBCT}$ has higher intensity than $PI\_CBCT_{segCBCT}$. Whether reducing noise and artifacts can improve the translation performance in boundary area still needs further study.

Chapter 4 Discussion and Conclusion

In this study, pulmonary perfusion images were generated from CBCT and CT scans of 30 lung cancer patients using a cascading deep learning model. The results were quantitively analyzed both voxel-wise and function-wise. The CBCT-generated perfusion images achieved comparable accuracy with the CT-generated perfusion images, demonstrating that CBCT enhancement techniques can be used to improve the accuracy of CBCT-to-perfusion translation.

However, this study was limited to a dataset of only 30 cases, which may not fully represent the diverse spectrum of pathological conditions encountered in clinical practice and constrained the generalizability of the model. Pulmonary perfusion imaging inherently exhibits complex physiological variations, including heterogeneity in blood flow distribution—influenced by gravitational gradients and vascular branching patterns—as well as diverse pathological alterations such as hypoperfusion in emphysematous regions or localized perfusion abnormalities due to tumors (27,54). Consequently, the present findings may overlook certain complex scenarios that could arise when applying CBCT-based pulmonary perfusion generation in real clinical contexts. Furthermore, the performance of the pipeline could be sensitive to substantial variability in lung mask contours across different clinical CBCT datasets. Inaccuracies or inconsistencies in the lung masks may propagate through the subsequent steps of image enhancement and functional translation, potentially affecting the robustness of the final perfusion maps. Future

studies should prioritize the inclusion of larger, multi-institutional cohorts and develop more robust segmentation methods to handle the broad spectrum of clinical image quality and anatomical variation. On the other hand, the adoption of multi-institutional datasets inevitably introduces significant domain shifts. This shift arises from systematic variations in imaging protocols across different centers, such as differences in scan parameters, the use of disparate CBCT scanner models, and variations in post-processing algorithms. Such heterogeneity poses a substantial challenge, as a model trained predominantly on data from a single source may experience degraded performance when applied to data from a new site, thereby limiting its real-world clinical utility. Therefore, future research efforts must not only focus on expanding the sheer volume of training data but also proactively address the domain adaptation challenge. Promising directions include: (a) implementing data-level augmentation strategies, such as complex style transfer, to synthetically expand the domain space of the source data and simulate potential distribution shifts; (b) employing feature-level alignment methods to learn domain-invariant representations, thereby enhancing model stability against covariate shifts caused by differences in imaging protocols or equipment ; and (c) exploring lightweight model adaptation modules that allow for efficient, site-specific tuning with minimal local data, addressing both covariate and concept shifts encountered in new clinical deployments (55–57). These approaches are critical for transitioning the framework from a proof-of-concept demonstration to a reliable tool for real-world, multi-center clinical applications.

Secondly, a recognized limitation of this study is the lack of in-depth analysis regarding how inherent CBCT physical artifacts, such as scatter radiation and beam hardening, quantitatively impact the performance of the perfusion prediction model. These artifacts can degrade model performance through distinct mechanisms. Scatter radiation contributes to a global increase in noise and cupping artifacts, leading to inaccuracies and non-uniformity in CT numbers across the image. This is particularly detrimental in lung tissue, where low density amplifies these effects, potentially causing the model to misinterpret anatomical or functional information. Research specifically investigating multi-source CBCT systems confirms that scatter is a primary cause of CT number inaccuracy and reduced contrast, which would directly challenge any intensity-based prediction task (58). On the other hand, beam hardening introduces streaking artifacts and causes shifts in CT values, especially at tissue boundaries and around high-density objects. This can alter the perceived contrast between different tissues, potentially misleading the model's feature extraction process in critical regions. Therefore, future work can integrate advanced physics-based correction algorithms (e.g., Monte Carlo-based scatter correction) into the data preprocessing process to isolate and quantify the individual and combined impact of these artifacts on the model’s output. However, it is crucial to consider that while correction algorithms restore physical accuracy, they may also inadvertently suppress unique but legitimate local image textures. This loss of detail or alteration of the native data distribution could increase the discrepancy between the generated perfusion images and the ground truth. A

balanced approach would involve comparative studies using corrected and uncorrected data to evaluate whether artifact removal leads to a net improvement in model performance.

Thirdly, registration errors between CBCT and SPECT perfusion images represent a critical factor compromising the quality of generated outputs. Respiratory motion induces dynamic deformation in the lung region across separate scanning sessions. Even with respiratory gating techniques, diaphragmatic displacement can exceed 2 cm, leading to misalignment in the basal lung regions (59). This challenge is exacerbated by the substantial difference in temporal resolution between CBCT (typically acquired within 1 minute) and SPECT (requiring $15-20$ min for acquisition), which results in the capture of inconsistent respiratory phases and introduces non-rigid deformation discrepancies. Furthermore, in pathological conditions such as pulmonary fibrosis or pleural adhesions, lung tissue exhibits altered biomechanical properties, amplifying registration inaccuracies particularly within diseased areas. These errors may obscure subtle perfusion defects, such as subsegmental pulmonary emboli, and thereby reduce the diagnostic accuracy of the results. While the current study employed registration algorithms available in 3D Slicer, future work should focus on developing advanced non-rigid registration methods capable of adapting to patient-specific pathological features.

Fourthly, the comparison between $PI\_CT_{segCBCT}$ and PI_CT_{segCT} illustrates the influence of the limited FOV of CBCT. To address this limitation, one compelling

strategy is to leverage high-quality planning CT to inform the CBCT segmentation. This could be achieved through advanced DIR techniques to propagate the meticulously defined CT lung mask onto the CBCT dataset, thereby effectively estimating the complete lung volume even in the presence of CBCT's limited field of view. This approach is clinically justified because although the planning CT cannot capture anatomical changes during radiotherapy treatment, the most significant changes—such as radiation-induced tumor shrinkage—typically occur within the tumor vicinity, which is already encompassed by the CBCT's FOV. It is therefore reasonable to assume that the peripheral lung anatomy, which the CT helps to delineate, remains relatively stable, thereby validating the feasibility of this propagation strategy. However, to translate this strategy into a robust clinical tool, future work should systematically analyze how the extent of lung coverage within the CBCT's FOV correlates with the accuracy of the perfusion generation. A criterion for minimum lung coverage is necessary to provide clear operational standards for model application in diverse clinical settings. Alternatively, deep learning models could be trained to directly synthesize a complete lung mask from a truncated CBCT scan, using paired CT-CBCT data as training ground truth (60). Moreover, the recent development of next-generation CBCT systems (e.g., Varian HyperSight (61)), which provide substantially improved image quality with lower noise and larger FOV, present a potential solution to these challenges. This technological leap may reduce the reliance on complex processing pipelines by providing inherently superior input data. Future work should validate our approach

utilizing these advanced platforms to fully leverage their potential.

Furthermore, a key observation from this study is that the generated perfusion images exhibited only a moderate voxel-level agreement with the ground truth, with performance being superior in low-functional regions compared to high-functional ones. This discrepancy may result from the complex and heterogeneous nature of vascular networks and blood flow in healthy, high-functional lung regions, which is more challenging for the deep learning model to capture accurately from the underlying CBCT anatomy. In contrast, low-functional areas, which often include pathologies or atelectasis, may present more simplified and homogeneous patterns that are easier to learn. This current limitation underscores that our model, in its present form, is not yet suitable for clinical applications requiring precise voxel-level quantification, such as dose escalation in high-functioning zones. However, the model's demonstrated ability to reliably identify broader patterns of functional impairment remains valuable. Future work will focus on improving model fidelity in high-functional areas through techniques such as employing loss functions that penalize errors in critical regions more heavily, and training on larger, more diverse datasets.

Finally, the evaluation of the generated images in this study may have over-relied on voxel-wise metrics, such as PSNR and SSIM, whose correlation with clinical significance is often limited. Furthermore, due to the size of dataset, function-wise metrics could not be thoroughly analyzed to identify potential patterns from the

limited data. However, radiologists place greater emphasis on the discernibility of diagnostically critical regions, such as the filling status of segmental-level pulmonary arteries and the morphological features of perfusion defect areas (27). While the generated images might perform adequately in terms of voxel-wise metrics, they could exhibit distortions in local diagnostic features. A critical step for clinical translation is to define what constitutes a clinically acceptable agreement for these functional images, which will require future validation with clinical outcome data. Towards this goal, subsequent research should adopt task-oriented evaluation strategies. For example, generated images could be fed into a pulmonary embolism classification model, using the changes in AUC as a criterion for generation quality. Additionally, dosimetric impact represents a core evaluation dimension in radiotherapy. A practical clinical workflow could leverage such CBCT-derived functional images for adaptive therapy: during treatment, automatically generated ventilation and perfusion maps would be fused to provide a comprehensive functional profile. This would allow clinicians to visually assess and quantitatively evaluate functional lung changes, and if significant, trigger plan adaptation to dynamically spare high-functioning regions. The ultimate test for clinical utility will be whether these images can lead to meaningful improvements in dosimetric parameters (e.g., fMLD, V20) and, ultimately, a reduction in radiation-induced lung toxicity.

In summary, although this study did not achieve ideal outcomes due to data

limitations and model adaptation issues, it helped to illuminate the key challenges associated with CBCT-based pulmonary perfusion image generation. These findings provide valuable guidance for future research and suggest the potential application of CBCT-based perfusion images generation in FLART.

References

1. Wild CP, Weiderpass E, Stewart BW, editors. World Cancer Report: Cancer research for cancer prevention [Internet]. Lyon (FR): International Agency for Research on Cancer; 2020 [cited 2024 Dec 16]. (IARC World Cancer Reports). Available from: http://www.ncbi.nlm.nih.gov/books/NBK606505/

2. Marks LB, Yu X, Vujaskovic Z, Small W, Folz R, Anscher MS. Radiation-induced lung injury. Semin Radiat Oncol. 2003 Jul 1;13(3):333–45.

3. Marks LB, Spencer DP, Sherouse GW, Bentel G, Clough R, Vann K, et al. The role of three dimensional functional lung imaging in radiation treatment planning: The functional dose-volume histogram. Int J Radiat Oncol. 1995 Aug 30;33(1):65–75.

4. Hoover DA, Capaldi DP, Sheikh K, Palma DA, Rodrigues GB, Dar AR, et al. Functional lung avoidance for individualized radiotherapy (FLAIR): study protocol for a randomized, double-blind clinical trial. BMC Cancer. 2014 Dec 11;14(1):934.

5. Siva S, Thomas R, Callahan J, Hardcastle N, Pham D, Kron T, et al. High-resolution pulmonary ventilation and perfusion PET/CT allows for functionally adapted intensity modulated radiotherapy in lung cancer. Radiother Oncol. 2015 May 1;115(2):157–62.

6. Allen AM, Albert M, Caglar HB, Zygmanski P, Soto R, Killoran J, et al. Can Hyperpolarized Helium MRI add to radiation planning and follow-up in lung cancer? J Appl Clin Med Phys. 2011;12(2):169–83.

7. Thomas HMT, Zeng J, Lee J Howard J, Sasidharan BK, Kinahan PE, Miyaoka RS, et al. Comparison of regional lung perfusion response on longitudinal MAA SPECT/CT in lung cancer patients treated with and without functional tissue-avoidance radiation therapy. Br J Radiol. 2019 Nov 1;92(1103):20190174.

8. Seppenwoolde Y, Muller SH, Theuws JCM, Baas P, Belderbos JSA, Boersma LJ, et al. Radiation dose-effect relations and local recovery in perfusion for patients with non–small-cell lung cancer. Int J Radiat Oncol. 2000 Jun 1;47(3):681–90.

9. West JB. Ventilation-Perfusion Relationships. Am Rev Respir Dis. 1977 Nov;116(5):919–43.

10. Siva S, Devereux T, Ball DL, MacManus MP, Hardcastle N, Kron T, et al. Ga-68 MAA Perfusion 4D-PET/CT Scanning Allows for Functional Lung Avoidance Using Conformal Radiation Therapy Planning. Technol Cancer Res Treat. 2016 Feb 1;15(1):114–21.

11. Radiation effects on the respiratory system | British Journal of Radiology | Oxford

Academic. [cited 2024 Dec 16]; Available from: https://academic.oup.com/bjr/article-abstract/78/Supplement_27/75/7485758

12. Ireland RH, Tahir BA, Wild JM, Lee CE, Hatton MQ. Functional Image-guided Radiotherapy Planning for Normal Lung Avoidance. Clin Oncol. 2016 Nov 1;28(11):695–707.

13. Meng X, Frey K, Matuszak M, Paul S, Ten Haken R, Yu J, et al. Changes in Functional Lung Regions During the Course of Radiation Therapy and Their Potential Impact on Lung Dosimetry for Non-Small Cell Lung Cancer. Int J Radiat Oncol. 2014 May 1;89(1):145–51.

14. Vinogradskiy YY, Castillo R, Castillo E, Chandler A, Martel MK, Guerrero T. Use of weekly 4DCT-based ventilation maps to quantify changes in lung function for patients undergoing radiation therapy. Med Phys. 2012;39(1):289–98.

15. Woodruff HC, Shieh CC, Hegi-Johnson F, Keall PJ, Kipritidis J. Quantifying the reproducibility of lung ventilation images between 4-Dimensional Cone Beam CT and 4-Dimensional CT. Med Phys. 2017;44(5):1771–81.

16. Kipritidis J, Hugo G, Weiss E, Williamson J, Keall PJ. Measuring interfraction and intrafraction lung function changes during radiation therapy using four-dimensional cone beam CT ventilation imaging. Med Phys. 2015;42(3):1255–67.

17. Zhang J, Ma J, Zhou S, Hubbs JL, Wong TZ, Folz RJ, et al. Radiation-Induced Reductions in Regional Lung Perfusion: 0.1–12 Year Data From a Prospective Clinical Study. Int J Radiat Oncol. 2010 Feb 1;76(2):425–32.

18. Bradley JD, Hope A, El Naqa I, Apte A, Lindsay PE, Bosch W, et al. A Nomogram to Predict Radiation Pneumonitis, Derived From a Combined Analysis of RTOG 9311 and Institutional Data. Int J Radiat Oncol. 2007 Nov 15;69(4):985–92.

19. Yamamoto T, Kabus S, Bal M, Bzdusek K, Keall PJ, Wright C, et al. Changes in Regional Ventilation During Treatment and Dosimetric Advantages of CT Ventilation Image Guided Radiation Therapy for Locally Advanced Lung Cancer. Int J Radiat Oncol. 2018 Nov 15;102(4):1366–73.

20. Petersson J, Sánchez-Crespo A, Larsson SA, Mure M. Physiological imaging of the lung: single-photon-emission computed tomography (SPECT). J Appl Physiol. 2007 Jan;102(1):468–76.

21. Yin L, Shcherbinin S, Celler A, Thompson A, Fua TF, Liu M, et al. Incorporating Quantitative Single Photon Emission Computed Tomography into Radiation Therapy Treatment Planning for Lung Cancer: Impact of Attenuation and Scatter Correction on the Single Photon Emission Computed Tomography–Weighted Mean

Dose and Functional Lung Segmentation. Int J Radiat Oncol. 2010 Oct 1;78(2):587–94.

22. Yin LS, Tang L, Hamarneh G, Gill B, Celler A, Shcherbinin S, et al. Complexity and accuracy of image registration methods in SPECT-guided radiation therapy. Phys Med Biol. 2009 Dec;55(1):237.

23. Fox MS, Ouriadov A, Thind K, Hegarty E, Wong E, Hope A, et al. Detection of radiation induced lung injury in rats using dynamic hyperpolarized 129Xe magnetic resonance spectroscopy. Med Phys. 2014;41(7):072302.

24. Couch MJ, Ball IK, Li T, Fox MS, Ouriadov AV, Biman B, et al. Inert fluorinated gas MRI: a new pulmonary imaging modality. NMR Biomed. 2014;27(12):1525–34.

25. Tahir BA, Swift AJ, Marshall H, Parra-Robles J, Hatton MQ, Hartley R, et al. A method for quantitative analysis of regional lung ventilation using deformable image registration of CT and hybrid hyperpolarized gas/1H MRI. Phys Med Biol. 2014 Nov;59(23):7267.

26. Wild JM, Ajraoui S, Deppe MH, Parnell SR, Marshall H, Parra-Robles J, et al. Synchronous acquisition of hyperpolarised 3He and 1H MR images of the lungs – maximising mutual anatomical and functional information. NMR Biomed. 2011;24(2):130–4.

27. Hopkins SR, Wielpütz MO, Kauczor HU. Imaging lung perfusion. 2012 [cited 2024 Oct 13]; Available from: https://journals.physiology.org/doi/epdf/10.1152/japplphysiol.00320.2012

28. Tahir BA, Hughes PJC, Robinson SD, Marshall H, Stewart NJ, Norquay G, et al. Spatial Comparison of CT-Based Surrogates of Lung Ventilation With Hyperpolarized Helium-3 and Xenon-129 Gas MRI in Patients Undergoing Radiation Therapy. Int J Radiat Oncol. 2018 Nov 15;102(4):1276–86.

29. Hegi-Johnson F, Keall P, Barber J, Bui C, Kipritidis J. Evaluating the accuracy of 4D-CT ventilation imaging: First comparison with Technegas SPECT ventilation. Med Phys. 2017;44(8):4045–55.

30. Vinogradskiy Y, Jackson M, Schubert L, Jones B, Castillo R, Castillo E, et al. Assessing the use of 4DCT-ventilation in pre-operative surgical lung cancer evaluation. Med Phys. 2017;44(1):200–8.

31. Kipritidis J, Tahir BA, Cazoulat G, Hofman MS, Siva S, Callahan J, et al. The VAMPIRE challenge: A multi-institutional validation study of CT ventilation imaging. Med Phys. 2019;46(3):1198–217.

32. Liu Z, Miao J, Huang P, Wang W, Wang X, Zhai Y, et al. A deep learning method for

producing ventilation images from 4DCT: First comparison with technegas SPECT ventilation. Med Phys. 2020;47(3):1249–57.

33. Zhong Y, Vinogradskiy Y, Chen L, Myziuk N, Castillo R, Castillo E, et al. Technical Note: Deriving ventilation imaging from 4DCT by deep convolutional neural network. Med Phys. 2019;46(5):2323–9.

34. Kipritidis J, Siva S, Hofman MS, Callahan J, Hicks RJ, Keall PJ. Validating and improving CT ventilation imaging by correlating with ventilation 4D-PET/CT using 68Ga-labeled nanoparticles. Med Phys. 2014;41(1):011910.

35. Castillo E, Nair G, Turner-Lawrence D, Myziuk N, Emerson S, Al-Katib S, et al. Quantifying pulmonary perfusion from noncontrast computed tomography. Med Phys. 2021;48(4):1804–14.

36. Ren G, Zhang J, Li T, Xiao H, Cheung LY, Ho WY, et al. Deep Learning-Based Computed Tomography Perfusion Mapping (DL-CTPM) for Pulmonary CT-to-Perfusion Translation. Int J Radiat Oncol. 2021 Aug 1;110(5):1508–18.

37. Ren G, Li B, Lam S kit, Xiao H, Huang YH, Cheung AL yin, et al. A Transfer Learning Framework for Deep Learning-Based CT-to-Perfusion Mapping on Lung Cancer Patients. Front Oncol [Internet]. 2022 Jul 1 [cited 2024 Dec 16];12. Available from: https://www.frontiersin.org/journals/oncology/articles/10.3389/fonc.2022.883516/full

38. Scarfe WC, Farman AG. What is Cone-Beam CT and How Does it Work? Dent Clin North Am. 2008 Oct 1;52(4):707–30.

39. Vergalasova I, Cai J. A modern review of the uncertainties in volumetric imaging of respiratory-induced target motion in lung radiotherapy. Med Phys. 2020;47(10):e988–1008.

40. Stankovic U, Ploeger LS, van Herk M, Sonke JJ. Optimal combination of anti-scatter grids and software correction for CBCT imaging. Med Phys. 2017;44(9):4437–51.

41. Rusanov B, Hassan GM, Reynolds M, Sabet M, Kendrick J, Rowshanfarzad P, et al. Deep learning methods for enhancing cone-beam CT image quality toward adaptive radiation therapy: A systematic review. Med Phys. 2022;49(9):6019–54.

42. Jensen KR, Brink C, Hansen O, Bernchou U. Ventilation measured on clinical 4D-CBCT: Increased ventilation accuracy through improved image quality. Radiother Oncol. 2017 Dec 1;125(3):459–63.

43. Liu Z, Tian Y, Miao J, Men K, Wang W, Wang X, et al. Deriving Pulmonary Ventilation Images From Clinical 4D-CBCT Using a Deep Learning-Based Model. Front Oncol [Internet]. 2022 May 2 [cited 2024 Dec 16];12. Available from:

https://www.frontiersin.org/journals/oncology/articles/10.3389/fonc.2022.889266/full

44. Lam YL, Lam SK, Cheung LY, Ho WY, Kong FM, Cai J, et al. The Feasibility of CBCT Based Pulmonary Perfusion Imaging Via Cascaded Deep Learning Framework for Functionally Guided Adaptive Radiation Therapy. In AAPM; 2023 [cited 2024 Dec 16]. Available from: https://aapm.confex.com/aapm/2023am/meetingapp.cgi/Paper/4837

45. Klein S, Staring M, Murphy K, Viergever MA, Pluim JPW. elastix: A Toolbox for Intensity-Based Medical Image Registration. IEEE Trans Med Imaging. 2010 Jan;29(1):196–205.

46. Shamonin DP, Bron EE, Lelieveldt BPF, Smits M, Klein S, Staring M. Fast Parallel Image Registration on CPU and GPU for Diagnostic Classification of Alzheimer's Disease. Front Neuroinformatics [Internet]. 2014 Jan 16 [cited 2024 Dec 16];7. Available from: https://www.frontiersin.org/journals/neuroinformatics/articles/10.3389/fninf.2013.00050/full

47. Kikinis R, Pieper SD, Vosburgh KG. 3D Slicer: A Platform for Subject-Specific Image Analysis, Visualization, and Clinical Support. In: Jolesz FA, editor. Intraoperative Imaging and Image-Guided Therapy [Internet]. New York, NY: Springer; 2014 [cited 2024 Dec 16]. p. 277–89. Available from: https://doi.org/10.1007/978-1-4614-7657-3_19

48. Hofmanninger J, Prayer F, Pan J, Röhrich S, Prosch H, Langs G. Automatic lung segmentation in routine imaging is primarily a data diversity problem, not a methodology problem. Eur Radiol Exp. 2020 Aug 20;4(1):50.

49. Tien HJ, Yang HC, Shueng PW, Chen JC. Cone-beam CT image quality improvement using Cycle-Deblur consistent adversarial networks (Cycle-Deblur GAN) for chest CT imaging in breast cancer patients. Sci Rep. 2021 Jan 13;11(1):1133.

50. Harms J, Lei Y, Wang T, Zhang R, Zhou J, Tang X, et al. Paired cycle-GAN-based image correction for quantitative cone-beam computed tomography. Med Phys. 2019;46(9):3998–4009.

51. Liu Y, Lei Y, Wang T, Fu Y, Tang X, Curran WJ, et al. CBCT-based synthetic CT generation using deep-attention cycleGAN for pancreatic adaptive radiotherapy. Med Phys. 2020;47(6):2472–83.

52. Gao L, Xie K, Wu X, Lu Z, Li C, Sun J, et al. Generating synthetic CT from low-dose cone-beam CT by using generative adversarial networks for adaptive radiotherapy. Radiat Oncol. 2021 Oct 14;16(1):202.

53. Weller A, Dunlop A, Oxer A, Gunapala R, Murray I, Gray MJ, et al. Spect perfusion imaging versus CT for predicting radiation injury to normal lung in lung cancer patients. Br J Radiol. 2019 Sep 1;92(1101):20190184.

54. Powers KA, Dhamoon AS. Physiology, Pulmonary Ventilation and Perfusion. In: StatPearls [Internet]. Treasure Island (FL): StatPearls Publishing; 2025 [cited 2026 Jan 19]. Available from: http://www.ncbi.nlm.nih.gov/books/NBK539907/

55. Matta S, Lamard M, Zhang P, Guilcher AL, Borderie L, Cochener B, et al. A systematic review of generalization research in medical image classification. Comput Biol Med. 2024;183:109256.

56. Yoon JS, Oh K, Shin Y, Mazurowski MA, Suk HI. Domain Generalization for Medical Image Analysis: A Review. Proc IEEE. 2024;112(10):1583–609.

57. Xue Z, Yang F, Rajaraman S, Zamzmi G, Antani S. Cross Dataset Analysis of Domain Shift in CXR Lung Region Detection. Diagnostics [Internet]. 2023;13(6). Available from: https://www.mdpi.com/2075-4418/13/6/1068

58. Deng W, Tian S, Dai J, Kang J, He T, Zhou L, et al. A preliminary study of characteristics of cross scattering for multi-source cone-beam CT. Med Phys. 2025 Nov;52(11):e70133.

59. Keall PJ, Mageras GS, Balter JM, Emery RS, Forster KM, Jiang SB, et al. The management of respiratory motion in radiation oncology report of AAPM Task Group 76 a. Med Phys. 2006;33(10):3874–900.

60. Xie K, Gao L, Xi Q, Zhang H, Zhang S, Zhang F, et al. New technique and application of truncated CBCT processing in adaptive radiotherapy for breast cancer. Comput Methods Programs Biomed. 2023;231:107393.

61. Varian. HyperSight | Varian [Internet]. 2025 [cited 2026 Jan 15]. Available from: https://www.varian.com/products/radiotherapy/treatment-delivery/hypersight